Int. J. Electrochem. Sci., 17 **(2022)** Article Number: 221234, doi: 10.20964/2022.12.28

International Journal of
ELECTROCHEMICAL
SCIENCE
www.electrochemsci.org

Preparation of Fe-doped $Na_2Mn_3O_7$ and its Application as a Cathode Material for Sodium-ion Batteries

Lunara Rakhymbay, Alibi Namazbay, Maksat Karlykan, Madina Abilkairova, Aishuak Konarov[*], *Zhumabay Bakenov*[*]

Department of Chemical and Materials Engineering, School of Engineering and Digital Sciences, Nazarbayev University, 53 Kabanbay Batyr Ave., Nur-Sultan 010000, Kazakhstan
[*]E-mail: aishuak.konarov@nu.edu.kz

Received: 15 September 2022 / *Accepted:* 10 October 2022 / *Published:* 30 November 2022

Rechargeable sodium-ion batteries are considered an alternative to Li-ion batteries in terms of large-scale grid storage applications. Finding a cathode material with excellent performance plays a vital role in batteries. Cation doping is one of the methods to stabilize the crystal structure of layered cathode materials for sodium-ion batteries (SIBs) and enhance their electrochemical performance. In this work, we studied the effect of Fe doping on the properties of the $Na_2Fe_xMn_{2-x}O_7$ (x=0.0, 0.5) layered material, which was synthesized via a conventional solid-state method at 600 °C. The X-ray diffraction (XRD) analysis showed that the as-synthesized material was crystallized in a pure P2-type structure, except for the nondoped sample. The Fe-doped cathode samples delivered more stable cycle performance than a nondoped cathode material. An initial charge capacity of over 200 mAh g^{-1} was achieved for the Fe-doped electrode. Meanwhile, the nondoped electrode delivered approximately 90 mAh g^{-1} of initial charge capacity. After 25 continuous charge-discharge cycles at a constant current (20 mA g^{-1}), approximately 70% and 60% of the initial capacity remained for Fe-doped and nondoped electrodes, respectively.

Keywords: sodium-ion battery (SIB), layered cathode, solid-state method, Fe-doping, P2 structure

1. INTRODUCTION

Due to the growth of sustainable energy, transportation, and numerous mobile electronic devices, the demand for efficient and low-cost energy infrastructure has been increasing, which sparks interest in the development of new energy storage systems [1]**.** Although lithium-ion batteries (LIBs) have been dominating the market/commercial field because of their optimal electrochemical characteristics, the limited and unevenly distributed sources of lithium cannot maintain the rapidly expanding demand for batteries with a high specific capacity. Moreover, when a large-scale storage system that can maintain immense power output is introduced, drawbacks of lithium-based batteries restrain it from prevailing in

this sector, which encourages the search for suitable substitutes [2]. Sodium-ion batteries (SIBs) have emerged as promising alternatives to LIBs due to several determinant characteristics such as wide availability and a broad range of transition metals that can form electrochemically active cathode materials. Nevertheless, SIB cathode materials still underperform compared to their lithium-based counterparts in terms of cyclability [3]. The underlying cause is a larger ionic radius of Na+ (1.02 Å) in contrast to that of Li+ (0.76 Å), which negatively affects the charging/discharging rate for SIBs as opposed to LIBs and consequently decreases its cycle stability, longevity and energy density. Therefore, it prompts the deployment of hard carbon for SIBs as anode materials. In addition, graphite is utilized for LIBs, which makes SIBs have lower electrochemical potential of the cathode materials than LIBs. All of these factors compound the decreased working voltage of SIBs [4]. However, this apparent size difference between Na and Li ions provides a larger space in sodium compounds, which enables SIBs to eliminate the aforementioned shortcomings. In other words, lithium layered oxides ($LiCoO_2$ and $LiNiO_2$) can be synthesized from a small range of relatively high-cost transition metals such as cobalt and nickel, whereas sodium layered oxides can be formed from their wider spectra (Ti, Cr, Ni, Fe, Co, Mn) [5–8].

Among the explored cathode materials, some prospective candidates are layered transition metal oxides due to scalable synthesis techniques, high reversible capacity, and particular structures oriented in two dimensions [9–12]. One of them is $Na_2Mn_3O_7$, which exhibits worthwhile electrochemical results: minor voltage hysteresis between discharge and charge, large structural stability, and a relatively high level of capacity [13]. As a layered structure, $Na_2Mn_3O_7$ consists of two layers of Mn_3O_7 formed by MnO_6 octahedra links divided by sodium ions, which is analogous to the $NaMnO_2$ structure type [14,15], except the structure has 1/7 Mn vacancies, which encourage oxygen-redox capacity without jeopardizing the Mn-O bond [13]. However, layered transition metal oxides do not satisfy modern standards of batteries. This issue can be approached by reaching an anion redox reaction (ARR), but the strategy requires optimization of ARR stability, which can be implemented by doping a transition metal into a transition metal oxide; however, the doping modifies the structure, band gap, band structure and electrochemical characteristics, mainly the capacity and cyclability [16]. Recent research demonstrated that doping Mg^{2+} into $Na_2Mn_3O_7$ increased the rate capabilities and specific capacities because Mg^{2+} decreased the Na^+ vacancy ordering and enhanced the diffusion of sodium ions, so Mg-doped material had a high capacity of 143 mAh g^{-1} after 30 cycles [17]. Similarly, aluminum-doped $Na_2Mn_3O_7$ ($Na_{2.4}Al_{0.4}Mn_{2.6}O_7$) illustrates the increase in specific capacity to 215 mA h g^{-1} in the voltage window of 1.5-4.7 V at C/20 and relatively high cyclability at 40 cycles [18]. Titanium-doped $Na_2Mn_3O_7$ ($Na_2Ti_{0.5}Mn_{2.5}O_7$) increases its capacity retention by 79.1% after 60 cycles and has an adequate rate capability of 92.1 mAh g^{-1} at 0.5 A g^{-1}. Both results are associated with modifications in ARR and a reduction in O_2 emission during the redox reaction [19].

The P2-type structure was mentioned to demonstrate a cut above electrochemical performance due to stable ARR [20–22]. Iron, which is a low-cost, eco-friendly transition metal and has the characteristics of other dopant materials, was considered to achieve this type of structure in metal oxides. Na_xFeO_2 is considered a promising candidate for SIB cathode materials, but its capacity fading due to the unstable Fe^{4+} should be addressed [23,24].

In this research, the doping of iron on a triclinic $Na_2Mn_{3-x}Fe_xO_7$ layered transition metal oxide was conducted in search of a stable cathode material. The impact of the introduction of small proportional amounts of iron (x=0.5) on the electrochemical performance and structure of the cathode material was investigated. The findings in our research imply that Fe ions can improve the specific capacity and cyclability of the cathode material, which more notably positively affects the ARR. This new cathode material can become a key player in the "green" design of the new generation of SIBs.

2. EXPERIMENTAL PROCEDURE

2.1 Material synthesis

The targeted compounds were synthesized through a solid-state reaction by mixing powdered reactants, pressing them into pellets, and annealing them in a muffle furnace for the desired time. The precursors $NaNO_3$, $Mn(NO_3)_2$, and $Fe(NO_3)_3$ with a purity of ≥ 99%, which were purchased from Sigma Aldrich, were ground together in a mortar using a pestle according to the stoichiometric ratio. The amount of $Fe(NO_3)_3$ in the initial powder mixture was adjusted to x = 0.0 and 0.5 in $Na_2Mn_{3-x}Fe_xO_7$. After being thoroughly mixed, the powder was pressed into a pellet. Then, the pellet was placed in an alumina crucible, transferred to a muffle furnace in open air and heated at 600℃ for 5 hours with a heating rate of 10℃/min for the annealing reaction to proceed. After it had naturally cooled in the furnace to room temperature, the dark-brown powder was retrieved from the furnace and kept in an argon glovebox for future analysis.

2.2 Characterization of as-synthesized materials

To evaluate the phase purity and crystal structure of the synthesized compound, XRD analysis was obtained using XRD Rigaku SmartLab (Core facilities, Nazarbayev University). The parameters of XRD were set to begin with 2θ=10-70° with a step of 0.02° and a speed of 7°/minute.

X-ray photoelectron spectroscopy (XPS, Core facilities, Nazarbayev University) was performed by applying NEXSA G2 XPS, which offers a fully automated study of sample surfaces with several methods. NEXSA G2 XPS was configured to have a sampling area of 3500 mm^2, a thickness of 20 mm, a voltage of 220 V, a frequency of 50 Hz, an X-ray spot size of 350 μm, and a static magnetic field at 45 μT.

A Crossbeam 540 microscope was used for scanning electron microscopy (SEM), energy dispersive spectroscopy (EDS) (Core facilities, Nazarbayev University) and JEM 1400Plus transmission electron microscopy (TEM, Core facilities, Nazarbayev University) to investigate the morphology of the samples. Additionally, inductively coupled plasma optical emission spectroscopy (ICP–OES, Core facilities, Nazarbayev University), a footprint elemental analysis technique, was applied to obtain and quantify the metal ion content in the material.

2.3 Electrochemical performance

To evaluate the electrochemical properties of the materials, the active cathode materials were blended with acetylene black (98% purity, MTI Corp.) and polyvinylidene difluoride (PVDF, 98% purity, Sigma–Aldrich) in N-methyl pyrrolidinone (98%, Sigma–Aldrich) as a solvent in a weight ratio of 8:1:1. After homogenous mixing, the resulting slurry was applied to aluminum foil (MTI Corp.) using the doctor-blade method. The casted slurry was dried in a vacuum oven at 120℃ for 8 h. Then, the electrode was rolled and punched into a circular disk with a diameter of 14 mm and served as a cathode for SIBs. Electrodes were individually weighed and incorporated into half-cells. The half-cell assembly was conducted in an argon glovebox (Inilab, Germany) with an inert atmosphere filled with argon (O_2 ≤0.1 ppm and H_2O ≤0.1 ppm) to avoid exposure to moisture and oxygen (particularly with sodium). The half-cell consists of the CR2032 coin cell type. The electrode in the coin cell was a solution of propylene carbonate with fluoroethylene carbonate (98:2) in 0.5-M sodium hexafluorophosphate.

2.4 Electrochemical measurements

Cyclic voltammetry (CV) data were collected from a Biologic SAS VMP-3 electrochemical tester. To examine the cathode material capacity and cyclability, galvanostatic cycling of the half-cell was performed over a specific voltage window of 1.5–4.7 V utilizing a multichannel battery tester "BT-2000 Arbin" at a C rate of 0.1.

3. RESULTS AND DISCUSSION

The crystal structures of the synthesized pristine and Fe-doped samples were studied using XRD patterns, which are shown in Fig. 1. The observable peaks of $Na_2Mn_3O_7$ have indexed to their corresponding crystal structure in Fig. 1. These peaks confirm that the material was crystallized in the triclinic phase with a $P\bar{1}$ space group. All diffraction peaks of the pristine material were consistent with previous reports [15]. In contrast, the XRD patterns of the Fe-doped material revealed different peaks. From the results, the materials crystallized into different crystal structures, unlike the bare compound. Therefore, the Fe-doped compound can be indexed as a hexagonal phase with the space group $P6_3/mmc$, and other impurity peaks were not observed. When Fe was introduced to the crystal structure, the intensity of the peaks decreased, especially the peak at approximately 16 degrees, which indicates that it is more amorphous than the bare one.

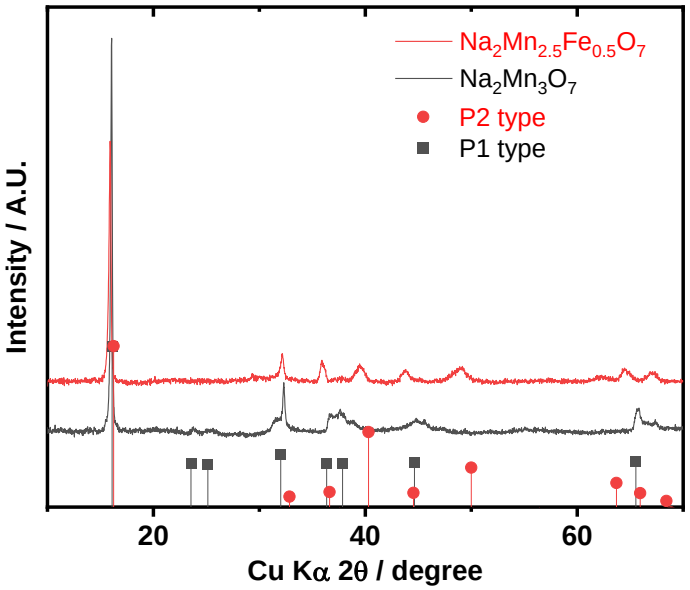

Figure 1. X-ray diffraction patterns of $Na_2Mn_{3-x}Fe_xO_7$ (x=0.0, 0.5)

Scanning electron microscopy (SEM) was used to determine the morphology changes of particles between pristine and Fe-doped materials, and corresponding images are shown in Fig. 2. The undoped material shows an evenly distributed crystalline surface (Fig. 2a). With the introduction of iron, the particles have porous and irregular large crystal shapes, comprise well-outlined crystals, and exhibit agglomerated particles (Fig. 2b). Due to the higher impact of guest molecules on the active site and the good ability for the electrolyte to permeate, porous electrodes have exceptional electrocatalytic activity. The reason is that they ensure proper wettability, which enables a quick transfer of reactants and electrons.

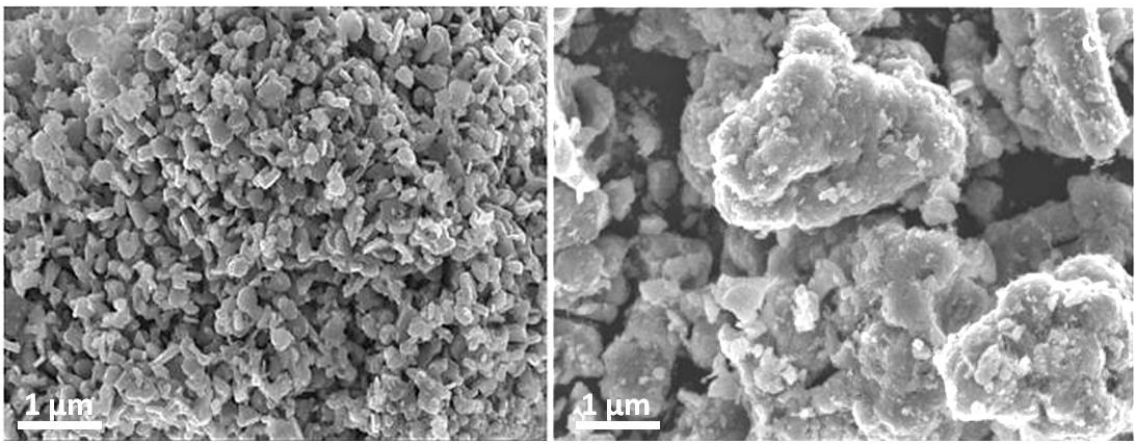

Figure 2. SEM images of the $Na_2Mn_{3-x}Fe_xO_7$: a) x=0, b) x= 0.5.

To determine the distribution of the elements in the sample, SEM–EDS was performed on the $Na_2Mn_{3-x}Fe_xO_7$ (x = 0.0, 0.5) samples, as shown in Figs. 2 and 3. The results demonstrate that the

distribution of the elements is homogenous in both compounds. Thus, Fe ions were successfully introduced to the crystal structure and well distributed.

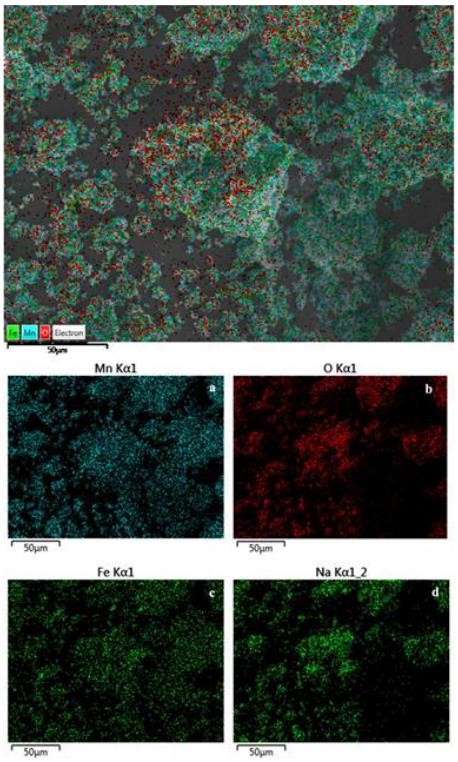

Figure 2. EDS mapping of the $Na_2Mn_3O_7$

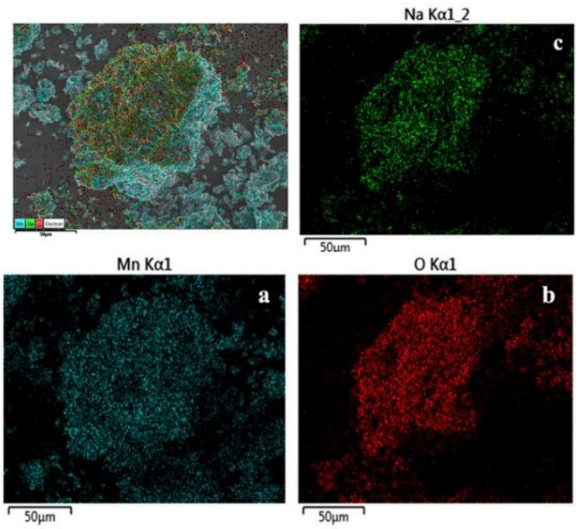

Figure 3. EDS mapping of the $Na_2Mn_{2.5}Fe_{0.5}O_7$

The exact cationic compositions were examined by ICP–OES analysis, and the results of molecular ratios are collected in Table 1. Before ICP analysis, the samples were dissolved fully without

forming a precipitate. For this experiment, a 50-mg sample before analysis was dissolved in a mixture of 37% hydrochloric acid and 70% nitric acid. Then, the dissolved solution was diluted to 100 ml with DI water. As shown, the molar ratio of each element in all samples is very similar to the initial formula. In summary, the elemental composition of EDS analysis corresponds to the ICP results.

Table 1. Results of ICP-OES

	Atomic Ratio		
Sample	Na/Mn	Na/Fe	Calculated formula
$Na_2Mn_{2.5}Fe_{0.5}O_7$	0.7479	3.56	$Na_{1.78}Mn_{2.38}Fe_{0.5}O_7$
$Na_2Mn_3O_7$	0.6428	0	$Na_{1.8}Mn_{2.8}O_7$

To determine the oxidation states of the elements in the pristine and Fe-doped materials, X-ray photoelectron spectroscopy (XPS) was performed. The results are displayed in Fig. 4. In the binding energy region of 705–740 eV, multiplet splitting appeared, which corresponds to the following orbitals: Fe $2p_{1/2}$ and Fe $2p_{3/2}$ (710.4 eV and 725 eV). The splitting of the two p orbital peaks of iron and satellite peaks is equal to 8.4 eV, which corresponds to iron with an oxidation state of 3+. The binding energy of the manganese valence electrons is in two regions: 642.5–655 eV duplets, which correspond to Mn $2p_{1/2}$ and Mn $2p_{3/2}$ with the oxidation state 4+ [18,25].

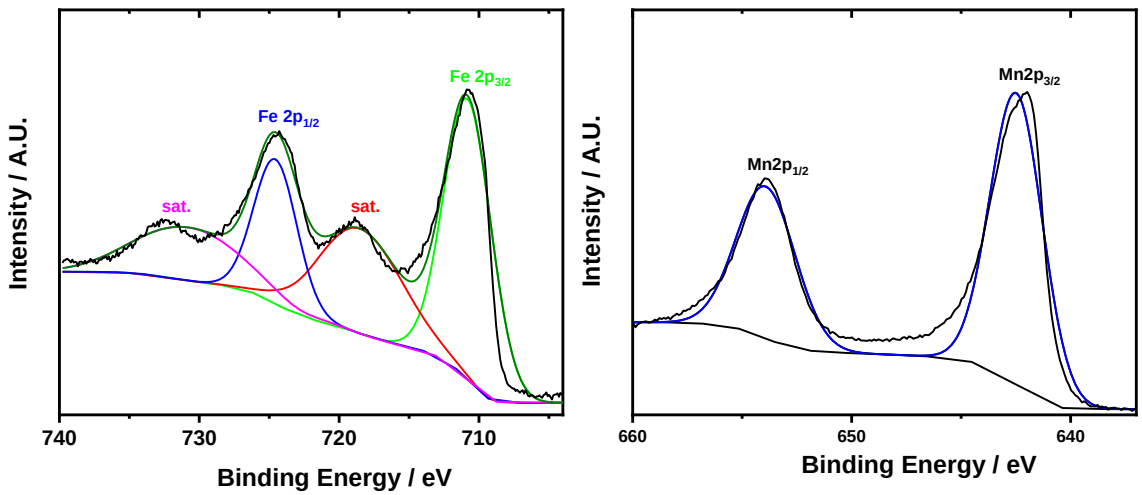

Figure 4. XPS analysis of $Na_2Mn_{2.5}Fe_{0.5}O_7$.

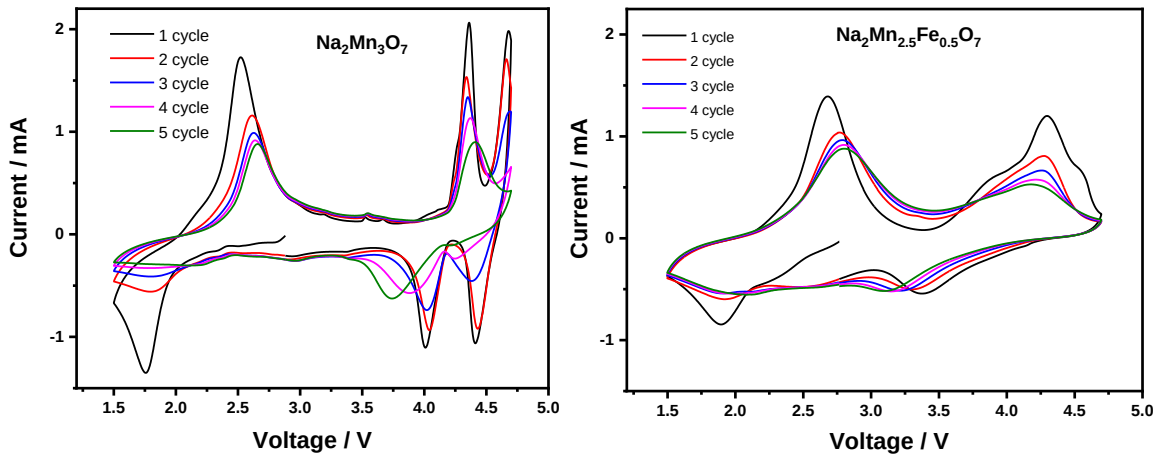

Figure 5. Cyclic voltammogram of $Na_2Mn_{3-x}Fe_xO_7$: a) x=0, and b) x= 0.5.

To understand the reaction proceeding in the electrode, a CV analysis was conducted on $Na_2Mn_{3-x}Fe_xO_7$ (x = 0, 0.5) in a potential range of 1.5-4.7 V at 0.1 mV s^{-1}. In case of $Na_2Mn_3O_7$, there are 3 main reversible peaks appeared during oxidation and reduction, which indicates the Mn^{3+}/Mn^{4+} and oxygen redox [13]. After 5 cycles, the intensity of the peaks decreased rapidly, specially at high voltage. On the other hand, $Na_2Mn_{3-x}Fe_xO_7$ electrode displayed two peaks, the first peak in the range of 1.5-2.7 V corresponds to the Mn^{3+}/Mn^{4+} redox couple. The second peak in the range of 3.0-3.7 V corresponds to the Fe^{3+}/Fe^{4+} redox couple. Here the same peak intensity decrease was observed, however less compared to the nondoped material.

The electrochemical performance of the $Na_2Mn_{3-x}Fe_xO_7$ (x = 0, 0.5) material was studied by constructing the half-cell configuration. The half-cells were cycled in the voltage range of 1.5–4.7 V at a current density of 20 mA g^{-1}. The bare $Na_2Mn_3O_7$ compound delivered an initial charge capacity of approximately 100 mAh g^{-1}, which was derived from oxygen redox, since the oxidation of Mn is 4+ and cannot be further oxidized in the normal voltage range. During discharge, oxygen was reduced, followed by the reduction of Mn^{4+} to Mn^{3+}, which delivered approximately 190 mAh g^{-1} of capacity. From the following cycles, the fast dropping of capacity was observed cycle by cycle. The electrochemical test data reveal that the cycle stability can be monotonously improved with the Fe doping content in $Na_2Mn_{2.5}Fe_{0.5}O_7$ compounds. The initial charge capacity above 200 mAh g^{-1} is delivered with the doped compound, which is double the delivery of the bare compound during the initial charge cycle. Moreover, it is favorable in terms of full-cell assembly because no presodiation process or additives are required. The delivered capacity was driven by oxygen and Fe^{3+} to Fe^{4+} oxidation. During discharge, a capacity of approximately 175 mAh g^{-1} was obtained. In the following 5 cycles, the capacity fading rate is much higher than that of the bare electrode.

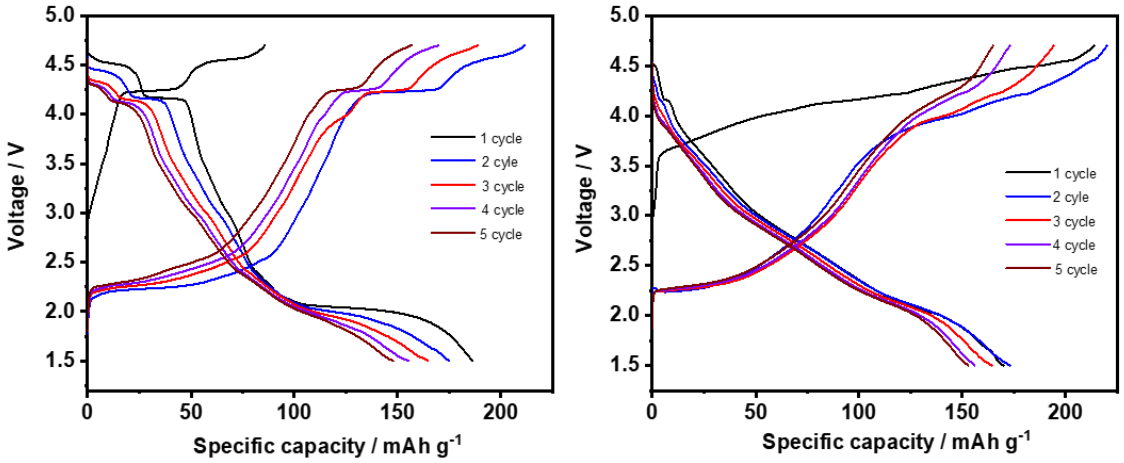

Figure 6. Charge-discharge profiles of $Na_2Mn_{3-x}Fe_xO_7$ in the voltage range of 1.5–4.7 V at a 20 mA g^{-1}: a) x=0, and b) x= 0.5

The cells were continuously cycled 25 times at a constant current. As Figure 7 shows, the Fe-doped electrode demonstrated better cycling performance by retaining approximately 70% of its initial capacity. Meanwhile, the capacity retention for bare electrodes after 25 cycles was approximately 60%. Thus, Fe doping can significantly enhance the capacity retention by stabilizing the crystal structure of $Na_2Mn_{2.5}Fe_{0.5}O_7$. Among the reported studies, which are shown in Table 2, the retention of the capacity is not attractive, however, need to pay attention on the voltage range that cells are cycled. At high voltage, the batteries tend to degrade faster.

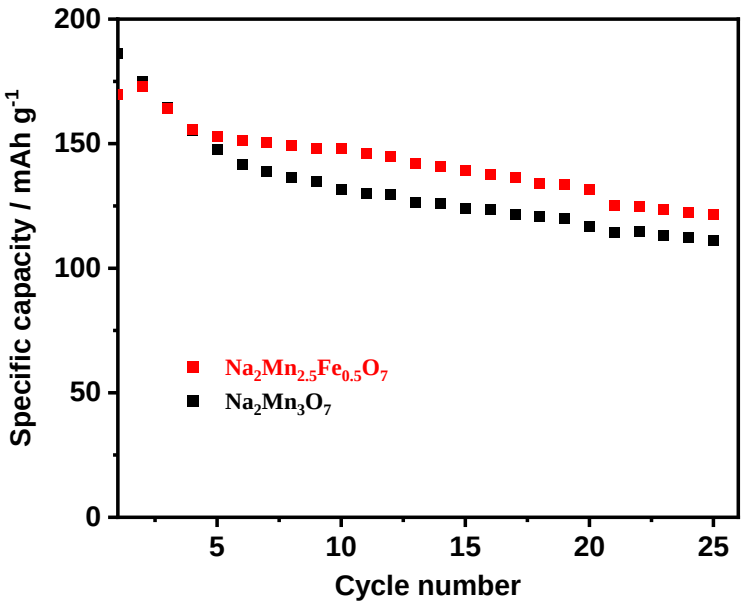

Figure 7. Cycling performance of the cathode materials in the voltage range of 1.5–4.7 V at 20 mA g^{-1}

Table 2. Comparison of the Fe/Mn based cathodes

Material	**Initial discharge capacity / mAh g^{-1}**	**Capacity retention / % (cycle)**	**Voltage range / V**	**Ref.**
O3-$Na_{2/3}Fe_{2/3}Mn_{1/3}O_2$	157	78 (15)	1.5 – 4.2	[10]
P2-$Na_{2/3}Fe_{2/3}Mn_{1/3}O_2$	151	80 (15)	1.5 – 4.2	[10]
P2-$Na_{0.67}Fe_{0.5}Mn_{0.5}O_2$	105	85 (30)	1.5 – 4.3	[11]
P2-$Na_{0.67}Fe_{0.5}Mn_{0.5}O_2$	125	40 (30)	1.5 – 4.3	[11]
O3-$Na_{2/3}Fe_{1/2}Mn_{1/2}O_2$	130	88 (25)	2.0 – 4.0	[12]
P2- $Na_{2/3}Fe_{1/2}Mn_{1/2}O_2$	115	78 (25)	2.0 – 4.0	[12]
$Na_{0.5}Fe_{0.5}Mn_{0.5}O_2$	130	85.4 (30)	1.5 – 4.0	[21]
$Na_{0.5}[Li_{0.05}(Fe_{0.5}Mn_{0.5})_{0.95}]O_2$	135	90 (30)	1.5 – 4.0	[21]
$Na_{0.5}[Li_{0.1}(Fe_{0.5}Mn_{0.5})_{0.9}]O_2$	145	93 (30)	1.5 – 4.0	[21]
$Na_{0.5}[Li_{0.2}(Fe_{0.5}Mn_{0.5})_{0.8}]O_2$	130	95 (30)	1.5 – 4.0	[21]
$Na_2Mn_{2.5}Fe_{0.5}O_7$	175	70 (25)	1.5 – 4.7	This work

4. CONCLUSION

In summary, we investigated the effect of Fe ion doping on the $Na_2Mn_{3-x}Fe_xO_7$ (x=0.0, 0.5) layered cathode material. XRD data revealed that when the materials were doped with Fe, they preferred to be crystallized in a P2-type structure to a P1-type structure. The electrochemical performance showed that the introduction of Fe increased the initial charge capacity, which is favorable in the full-cell configuration. In terms of cyclability, the doped electrode presented better cycling performance than the bare electrode by retaining 70% of the initial capacity. Currently, the materials are being deeply studied with state-of-the-art techniques, and the results will be published soon.

ACKNOWLEDGMENT
This work was supported by the Ministry of Education and Science of the Republic of Kazakhstan Grant (AP08856179) and by the Nazarbayev University Faculty-Development Competitive Research Grant (080420FD1914). A.K. thanks the Social Policy Grant awarded to him by the NU.

References

1. J.Y. Hwang, S.T. Myung, Y.K. Sun, *Chem. Soc. Rev.*, 46 (2017) 3529–3614.
2. K. Kubota, S. Komaba, *J. Electrochem. Soc.*, 162 (2015) A2538–A2550.
3. N. Yabuuchi, K. Kubota, M. Dahbi, S. Komaba, *Chem. Rev.*, 114 (2014) 11636–11682.
4. D. Karabelli, S. Singh, S. Kiemel, J. Koller, A. Konarov, F. Stubhan, R. Miehe, M. Weeber, Z. Bakenov, K.P. Birke, *Front. Energy Res.*, 8 (2020) 1–16.
5. N. Voronina, H.J. Kim, A. Konarov, N. Yaqoob, K.S. Lee, P. Kaghazchi, O. Guillon, S.T. Myung, *Adv. Energy Mater.*, 11 (2021) 1–12.
6. N. Voronina, J.H. Jo, J.U. Choi, A. Konarov, J. Kim, S.T. Myung, *J. Power Sources* (2020).
7. A. Konarov, H.J. Kim, N. Voronina, Z. Bakenov, S.T. Myung, *ACS Appl. Mater. Interfaces*, 11

(2019) 28928–28933.
8. S. Birgisson, T.L. Christiansen, B.B. Iversen, *Chem. Mater.*, 30 (2018) 6636–6645.
9. B.C. Saha, A.K. Bera, S.M. Yusuf, *ACS Appl. Energy Mater.*, 4 (2021) 6040–6054.
10. E. Gonzalo, M.H. Han, J.M. López Del Amo, B. Acebedo, M. Casas-Cabanas, T. Rojo, *J. Mater. Chem. A*, 2 (2014) 18523–18530.
11. D. Nayak, S. Ghosh, A. Venimadhav, *Ionics (Kiel).*, 27 (2021) 2421–2430.
12. M.H. Han, B. Acebedo, E. Gonzalo, P.S. Fontecoba, S. Clarke, D. Saurel, T. Rojo, *Electrochim. Acta*, 182 (2015) 1029–1036.
13. B. Mortemard de Boisse, S. Nishimura, E. Watanabe, L. Lander, A. Tsuchimoto, J. Kikkawa, E. Kobayashi, D. Asakura, M. Okubo, A. Yamada, *Adv. Energy Mater.*, 8 (2018) 1800409.
14. E.A. Raekelboom, A.L. Hector, J. Owen, G. Vitins, M.T. Weller, *Chem. Mater.*, 13 (2001) 4618–4623.
15. E. Adamczyk, V. Pralong, *Chem. Mater.*, 29 (2017) 4645–4648.
16. B. Song, M. Tang, E. Hu, O.J. Borkiewicz, K.M. Wiaderek, Y. Zhang, N.D. Phillip, X. Liu, Z. Shadike, C. Li, L. Song, Y.Y. Hu, M. Chi, G.M. Veith, X.Q. Yang, J. Liu, J. Nanda, K. Page, A. Huq, *Chem. Mater.*, 31 (2019) 3756–3765.
17. D.P. Siriwardena, J.F.S. Fernando, T. Wang, K.L. Firestein, C. Zhang, H.E.A. Brand, M.W.M. Jones, C.M. Kewish, P. Berntsen, T. Jenkins, C.E.M. Lewis, J.E. von Treifeldt, D.P. Dubal, D. V. Golberg, *Electrochim. Acta*, 394 (2021) 139139.
18. C. Soares, B. Silván, Y.S. Choi, V. Celorrio, V.R. Seymour, G. Cibin, J.M. Griffin, D.O. Scanlon, N. Tapia-Ruiz, *J. Mater. Chem. A*, 10 (2021) 7341–7356.
19. Y. Liu, C. Wang, M. Ren, H. Fang, Z. Jiang, F. Li, *J. Energy Chem.*, 63 (2021) 351–357.
20. C. Luo, A. Langrock, X. Fan, Y. Liang, C. Wang, *J. Mater. Chem. A*, 5 (2017) 18214–18220.
21. G.K. Veerasubramani, Y. Subramanian, M.S. Park, B. Senthilkumar, A. Eftekhari, S.J. Kim, D.W. Kim, *Electrochim. Acta*, 296 (2019) 1027–1034.
22. M. Ambrosetti, M.C. Mozzati, A. Cini, M. Fittipaldi, D. Spada, M. Sturini, I. Quinzeni, M. Bini, *Appl. Sci.*, 12 (2022) 1–18.
23. N. Yabuuchi, M. Kajiyama, J. Iwatate, H. Nishikawa, S. Hitomi, R. Okuyama, R. Usui, Y. Yamada, S. Komaba, *Nat. Mater.*, 11 (2012) 512–517.
24. L. Zhang, T. Yuan, L. Soule, H. Sun, Y. Pang, J. Yang, S. Zheng, *ACS Appl. Energy Mater.*, 3 (2020) 3770–3778.
25. S. Jia, J. Counsell, M. Adamič, A. Jonderian, E. McCalla, *J. Mater. Chem. A*, 10 (2022) 251–265.